

See discussions, stats, and author profiles for this publication at: <https://www.researchgate.net/publication/263939205>

# MAPbI<sub>3</sub>-xCl<sub>x</sub> Mixed Halide Perovskite for Hybrid Solar Cells: The Role of Chloride as Dopant on the Transport and Structural Properties

ARTICLE in CHEMISTRY OF MATERIALS · NOVEMBER 2013

Impact Factor: 8.35 · DOI: 10.1021/cm402919x

CITATIONS

180

READS

1,353

13 AUTHORS, INCLUDING:



**Tullo Besagni**

Italian National Research Council

37 PUBLICATIONS 529 CITATIONS

SEE PROFILE



**Aurora Rizzo**

Italian National Research Council

51 PUBLICATIONS 1,124 CITATIONS

SEE PROFILE



**Filippo De Angelis**

Università degli Studi di Perugia

265 PUBLICATIONS 11,207 CITATIONS

SEE PROFILE



**Roberto Mosca**

Italian National Research Council

130 PUBLICATIONS 1,053 CITATIONS

SEE PROFILE

# MAPbI<sub>3-x</sub>Cl<sub>x</sub> Mixed Halide Perovskite for Hybrid Solar Cells: The Role of Chloride as Dopant on the Transport and Structural Properties

Silvia Colella,<sup>†</sup> Edoardo Mosconi,<sup>‡</sup> Paolo Fedeli,<sup>§</sup> Andrea Listorti,<sup>\*,†,||</sup> Francesco Gazza,<sup>§,∇</sup> Fabio Orlandi,<sup>§,⊥</sup> Patrizia Ferro,<sup>§</sup> Tullio Besagni,<sup>§</sup> Aurora Rizzo,<sup>†</sup> Gianluca Calestani,<sup>§,⊥</sup> Giuseppe Gigli,<sup>†,||,#</sup> Filippo De Angelis,<sup>\*,‡</sup> and Roberto Mosca<sup>\*,§</sup>

<sup>†</sup>NNL—National Nanotechnology Laboratory, CNR Istituto Nanoscienze, Distretto Tecnologico, Via Arnesano 16, 73100 Lecce, Italy

<sup>‡</sup>Computational Laboratory for Hybrid/Organic Photovoltaics (CLHYO), CNR-ISTM, Via Elce di Sotto 8, I-06123 Perugia, Italy

<sup>§</sup>IMEM-CNR, Parco Area delle Scienze 37a, I-43124 Parma, Italy

<sup>||</sup>Center for Bio-Molecular Nanotechnology, Fondazione Istituto Italiano di Tecnologia, Via Barsanti, 73010 Arnesano (Lecce), Italy

<sup>⊥</sup>Department of Chemistry GIAF, University of Parma, Via Usberti 17/A, 43124, Parma, Italy

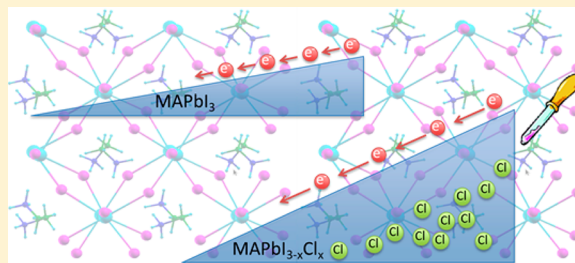
<sup>#</sup>Dipartimento di Matematica e Fisica “E. De Giorgi”, Università del Salento, Via per Arnesano, 73100 Lecce, Italy

<sup>∇</sup>Department of Chemistry “G. Ciamician”, University of Bologna, Via Selmi 2, 40126 Bologna, Italy

## Supporting Information

**ABSTRACT:** Hybrid halide perovskites represent one of the most promising solutions toward the fabrication of all solid nanostructured solar cells, with improved efficiency and long-term stability. This article aims at investigating the structural properties of iodide/chloride mixed-halide perovskites and correlating them with their photovoltaic performances. We found out that, independent of the components ratio in the precursor solution, Cl incorporation in an iodide-based structure, is possible only at relatively low concentration levels (below 3–4%). However, even if the material band gap remains substantially unchanged, the Cl doping dramatically improves the charge transport within the perovskite layer, explaining the outstanding performances of meso-superstructured solar cells based on this material.

**KEYWORDS:** perovskites, hybrid solar cells, X-ray structures, DFT investigations



## 1. INTRODUCTION

Finding viable alternatives to silicon-based photovoltaics, through low-cost solution processable materials, is crucial, when facing, as we are, a complex transition out of the fossil fuelled civilization.<sup>1,2</sup> The international scientific community constantly fosters the development of innovative solar energy transducing devices as outstanding performances have been reached nowadays in term of cell characteristics and stability.<sup>3–5</sup> However, for diverse reasons, these technologies have still not been scaled up. In this scenario, the utilization in nanostructured solar cells of an underexplored eclectic class of materials, the hybrid halide perovskites, has represented in 2012 a field breakthrough, allowing novel device architectures leading to record device performances,<sup>6–9</sup> thus holding the promise of cost-effective solar energy production. Hybrid halide perovskites were first investigated many years ago,<sup>10–13</sup> but in fact they have never been employed as active components of solar converting devices until very recently.<sup>14</sup> Among the first results of the pioneer works employing perovskites in solar cells, probably the most intriguing discovery concerned the perovskite concomitant capability of both absorbing light and

transporting charge within a mesoporous network. The application of a iodide/chloride mixed-halide perovskite CH<sub>3</sub>NH<sub>3</sub>PbI<sub>3-x</sub>Cl<sub>x</sub> (CH<sub>3</sub>NH<sub>3</sub> = MA) deposited on an inert Al<sub>2</sub>O<sub>3</sub> scaffold and coupled with a hole transporting material (HTM) showed outstanding performances up to 12.3%<sup>7,15</sup> in a so-called “meso-superstructured” solid state solar cells (SS-SC). In this conceptually innovative device, the charge transport properties of the active material are fundamental. In fact, for the absence of an acceptor medium (TiO<sub>2</sub>), after light absorption and charge separation the perovskite component is expected to support electron transport.

Despite the widening literature on the photovoltaic use of hybrid lead perovskites,<sup>6–9,16,17</sup> many questions, concerning their peculiar structural chemistry and material response to light induced processes, remain to be addressed. Since perovskite properties are likely to play a major role in impacting device performances, as well as foreseeing further advancements on

**Received:** August 30, 2013

**Revised:** October 18, 2013

**Published:** October 21, 2013



this emerging research front, the possibility to tune the perovskite features through composition control is very appealing. However, even if outstanding photovoltaic performances have been obtained using  $\text{MAPbI}_{3-x}\text{Cl}_x$ , little was said about the formation of this mixed halide perovskite, and the role of the chloride remains poorly investigated. Here we report a detailed investigation on Cl/I mixed halide lead methyl ammonium perovskites, and study the relation between the I:Cl ratio in the material and the SS-SC characteristics, aiming at optimizing device performances through composition tuning. We found out that the exact composition of the final compound does not reproduce the stoichiometry of the precursor solution. With those materials being self-assembling, their formation is based on the chemical complementarity and structural compatibility of the constituent atoms. During the assembling process the building blocks explore diverse possible configurations via weak bonding interactions aiming at the energetically most favorable one. Here we demonstrated, both experimentally and theoretically, that the formation of continuous solid phase  $\text{MAPbI}_{3-x}\text{Cl}_x$  is actually not allowed and that chloride incorporation into  $\text{MAPbI}_3$  is possible only at relatively low concentration, so that it could be classified as a dopant agent. Some experimental observations allowed us to rationalize the remarkable effect of this inclusion on the improvement of the charge mobility in the perovskite layer. We related the preparation protocol to the obtained structure/morphology, strengthening those findings with a detailed periodic DFT investigation on extended models. Additionally we employed these compounds as absorbing layers in SS-SC, rationalizing the device performances with the components effectively present in the active layer as a direct consequence of the synthetic procedure. Improving the knowledge of perovskite self-assembling process within a mesoporous structure could help in refining the material preparation strategy for the realization of better performing hybrid compounds toward higher device performances.

## 2. EXPERIMENTAL SECTION

**2.1. Material Preparation.** Lead halide hybrid perovskites were prepared by self-organization processes using different precursor solutions that were prepared by commercially available compounds. In particular,  $\text{PbCl}_2$  (Aldrich),  $\text{PbI}_2$  (Aldrich),  $\text{HCl}$  (37%) (Aldrich),  $\text{HI}$  (57%) (Aldrich),  $\text{CH}_3\text{NH}_2$  (41%) (Fluka), and  $\text{MACl}$  (Fluka) were used without further purification. The intermediate MAI compound was prepared by reactions of the amine aqueous solutions with  $\text{HI}$ , as previously reported.<sup>7,18</sup>

**Methyl Ammonium Lead Iodide Perovskite (PS1).**  $\text{MAPbI}_3$  perovskite was synthesized according to the procedure previously reported.<sup>18</sup> Equimolar mixtures of the as-synthesized MAI and  $\text{PbI}_2$  in  $\gamma$ -butyrolactone (99+%, Acros Organics) were stirred overnight at RT/60 °C to obtain a 20 wt % solution.

**Methyl Ammonium Lead Iodide Chloride (PS2).** The procedure described by Lee et al.<sup>7</sup> was followed. The precursor solution (20 wt %) was obtained by dissolving MAI and  $\text{PbCl}_2$  (3:1 molar ratio) in anhydrous  $N,N$ -dimethylformamide at room temperature.

**Lead Halide Mixture (PS3).**  $\text{MACl}$  and  $\text{PbI}_2$  (1:1 molar ratio) were dissolved in anhydrous  $N,N$ -dimethylformamide at room temperature to achieve a 20 wt % solution.

The PS1–3 perovskite films for XRD analysis were obtained by spin coating the solution on microscope glass slides at 1500 rpm for 45 s in nitrogen flux and then baking at 100 °C for 15 min (PS1), 45 min (PS2), or 10 min (PS3).

**2.2. Material Characterization. XRD Analysis.** XRD characterization was performed with a Thermo X'tra powder diffractometer equipped with  $\text{Cu K}\alpha$  radiation and a Thermo Electron Si(Li) solid

state detector. Diffraction pattern were collected by 0.05° 2 $\theta$  steps and counting times ranging from 2 to 10 s per step. In order to measure the XRD spectra of the perovskite powders, obtained films were carefully scratched from their substrate by an edged glass slide.

**UV–Vis Absorption.** Film absorbance spectra were measured in the 400–1000 nm range by a Jasco UV–vis V-530 spectrometer.

**2.3. Device Fabrication and Characterization.** FTO glasses (Pilkington, TEC15, 15 Ohm/sq) were etched with metallic Zn and  $\text{HCl}$  2 M. They were washed with water and cleaned in an ultrasonic bath in acetone and isopropanol for 10 min each. Then they were immersed in a 5:1:1 mixture of double distilled water,  $\text{H}_2\text{O}_2$  (30%), and  $\text{NH}_3$  (25%), for 10 min at 85 °C, followed by extensive rinsing in double distilled water to remove organic contamination. To make a compact  $\text{TiO}_2$  blocking layer of ca. 60 nm, the cleaned FTO glasses were coated with 0.15 M titanium diisopropoxide bis(acetylacetonate) (75% Aldrich) in 1-butanol (Aldrich) solution by spin-coating (2000 rpm), and then heated to 125 °C for 5 min. Afterwards, the coated film was cooled down to the room temperature, the same process was repeated twice with 0.3 M titanium diisopropoxide bis(acetylacetonate) solution in 1-butanol at 2000 rpm. The coated FTO glasses with  $\text{TiO}_2$  precursor solutions were heated at 450 °C for 15 min. A 0.6  $\mu\text{m}$  thick mesoporous  $\text{TiO}_2$  layer was deposited by spin-coating  $\text{TiO}_2$  paste (Dyesol 18NR-T) diluted further in terpineol at 1:2.5 by weight at 2000 rpm. The layers were then sintered in air to 450 °C for 1 h. Once cooled, 20 wt % perovskite precursor solutions were infiltrated into the mesoporous electrode film by spin-coating at 1500 rpm for 30 s in  $\text{N}_2$  atm. The coated films were then placed on a hot plate set at 100 °C for 15 min (PS1), 45 min (PS2), or 10 min (PS3). A chlorobenzene solution containing 31 mM Spiro-OMeTAD, 216 mM tert-butylpyridine, and 58 mM lithium bis(trifluoromethylsulfonyl)imide salt was cast onto the perovskite coated substrate and spun at a rate of 2500 rpm for 45 s. Cells were completed by thermal evaporation of 150 nm thick Ag electrodes. Both the perovskite and the HTM layers were deposited under inert atmosphere. Devices, with an active area between 0.025 and 0.045  $\text{mm}^2$ , were characterized in air under Air Mass 1.5 Global (AM 1.5 G) solar simulator with an irradiation intensity of 100  $\text{mW cm}^{-2}$ . The reported average values of the photovoltaic parameters were calculated over a series of 8–10 devices for each compound.

**2.4. DFT Calculations.** Periodic DFT calculations using the PBE exchange-correlation functional were performed on the tetragonal phase of the mixed halide  $\text{CH}_3\text{NH}_3\text{PbI}_{(3-x)}\text{Cl}_x$  materials. The simulation cell contains 32 repeated  $\text{CH}_3\text{NH}_3\text{PbI}_{(3-x)}\text{Cl}_x$  units (384 atoms), see Figure S3 in Supporting Information. The PWSCF code as implemented in the Quantum-Espresso program package<sup>19</sup> was used throughout. Electron–ion interactions were described by ultrasoft pseudopotentials with electrons from Pb 5d, 6s, 6p; N and C 2s, 2p; H 1s; I 5s, 5p; Br 4s, 4p; Cl 3s, 3s, shells explicitly included in the calculations. Calculations were performed within a scalar-relativistic (SR) approach. In selected cases we performed single point calculations on the SR-optimized geometries including spin–orbit coupling (SOC) effects.<sup>21</sup> All calculations were carried out at the  $\Gamma$  point of the Brillouin zone. Plane-wave basis set cutoffs for the smooth part of the wave functions and the augmented density of 25 and 200 Ry, respectively, were used. We carried out atomic and lattice parameters optimizations, starting from the experimental cell parameters reported for the tetragonal  $I4/mcm$   $\text{CH}_3\text{NH}_3\text{PbI}_3$  species.

## 3. RESULTS AND DISCUSSION

We investigated a series of hybrid lead perovskites, hereafter named PS1, PS2, and PS3, prepared by self-organization processes from three different precursor solutions and formed as both thin films on glass and sensitizers on  $\text{TiO}_2$  photoanodes. XRD analysis, reported in Figure 1, allowed us to identify PS1 thin films as  $\text{MAPbI}_3$  crystallized in the tetragonal perovskite structure<sup>14</sup> with lattice parameters  $a = 8.8755(5)$  Å and  $c = 12.6735(8)$  Å, as determined by a Le Bail profile refinement performed with the program GSAS.<sup>20</sup>

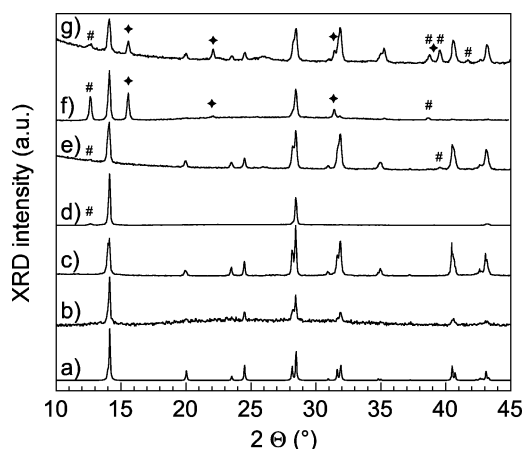


**Figure 1.** XRD pattern of PS1 (b) film and (c) powders, PS2 (d) films and (e) powders, PS3 (f) film and (g) powders. Diamonds indicate the peaks ascribed to  $\text{MAPbCl}_3$ , whereas the contribution of the  $\text{PbI}_2$  phase is indicated by hashes. (a) The  $\text{MAPbI}_3$  spectrum calculated from literature data.<sup>22</sup>

Comparison between PS1 films spectra and those of the powder obtained by carefully scratching the compound from glass substrates (Figure 1) shows that the films are poorly oriented. In contrast, the diffraction patterns of PS2 films show a high orientation (Figure 1d), so that only the reflection sequence related to the row of the reciprocal lattice normal to the film plane is observed. In agreement with the spectra reported by Lee et al. for the same material,<sup>7</sup> the (001) diffraction peak of  $\text{PbI}_2$  can also be detected with an intensity classifiable as an impurity phase. It is worth noting here that the presence of such a phase is expected to reduce the concentration of Pb ions available for perovskite formation, which could be expected to negatively affect the solar cell performances.

Analysis of the  $d$ -spacings related to the perovskite reflection sequence suggests that the PS2 main phase could be strictly related to  $\text{MAPbI}_3$ . To confirm this hypothesis the XRD analysis was repeated on the powder. Despite the obtained patterns being closely similar to those of PS1 (Figure 1), the diffraction profile in the multiplet regions presents a slight difference in the lattice parameters. Indeed the lattice parameters of the PS2 powder resulted in  $a = 8.8535(3)$  Å and  $c = 12.6434(4)$  Å, thus indicating ca. 0.7% reduction of the unit cell volume with respect to PS1 powders. Although small, this difference is not negligible, being well above the instrumental sensitivity, and it could be reasonably explained by hypothesizing a  $\text{MAPbI}_3$  structure presenting a certain level of Cl-doping. Thus,  $\text{CH}_3\text{NH}_3\text{PbI}_3$  formation is favored when the molar ratio I:Pb in the precursor solution is 3:1, the excess chloride and methylammonium being assumed to evaporate during the drying process.

To promote Cl incorporation we investigated the formation of the perovskite structure (PS3) using a 2:1 I:Pb molar ratio. The diffraction patterns show that PS3 films are highly oriented (Figure 1f), systematically pointing out the presence of Cl-doped  $\text{MAPbI}_3$  and  $\text{PbI}_2$  together with a further phase that was identified in the powdered samples as the cubic  $\text{MAPbCl}_3$ <sup>22</sup> (Figure 1g) with  $a = 5.683(2)$  Å. The segregation of the cubic  $\text{MAPbCl}_3$ , besides the Cl-doped  $\text{MAPbI}_3$  phase, indicates that the chloride solubility limit in the iodide derivative is quite low, in line with the unfavorable calculated formation energies,<sup>23</sup>

and that the formation of an extended solid solution is prevented which is likely due to the large difference in the ionic radii of  $\text{Cl}^-$  and  $\text{I}^-$  anions. Similar conclusions were drawn for Sn-based hybrid halide perovskites.<sup>24</sup> Thus, from XRD data we can argue that the perovskite composition cannot be widely tuned by varying the Cl:I molar ratio in the precursor solution, contrary to what is observed in Br/I mixed-halide perovskites.<sup>25</sup>

This deduction was further supported by optical absorption spectra recorded at room temperature. Indeed, all the considered films show roughly the same absorption edge at about 750 nm, which represents a usual feature in both  $\text{MAPbI}_3$ <sup>8,18,26</sup> and  $\text{MAPbI}_{3-x}\text{Cl}_x$ .<sup>7</sup> The Tauc plots (Figure 2)

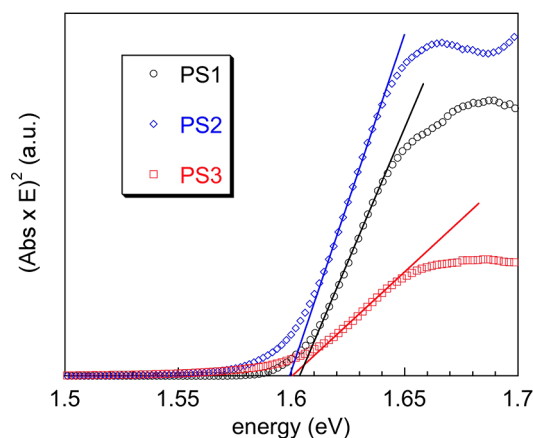


**Figure 2.** Tauc plots of PS1, PS2, and PS3 films.

reveal that the optical bandgap (EG) is  $1.60 \pm 0.01$  eV for all the films ( $\pm 0.01$  eV is the uncertainty referring to the spread of EG values for several sample films of each compound). The EG value obtained on  $\text{MAPbI}_3$  agrees with both experimentally measured data ranging from 1.57<sup>25,27</sup> to 1.63 eV,<sup>28</sup> and results from density functional theory (DFT) calculations.<sup>23</sup>

As for PS2 and PS3 films, based on results obtained on  $\text{MAPbI}_{3-x}\text{Br}_x$  and  $\text{MAPbBr}_{3-x}\text{Cl}_x$ , it was proposed that even in  $\text{MAPbI}_{3-x}\text{Cl}_x$  the optical absorption bands vary linearly with  $x$ .<sup>27</sup> Under this assumption and using for the bandgap of  $\text{MAPbCl}_3$  an EG a value of 3.11 eV,<sup>18</sup> we found that the measured EG uncertainty would correspond to  $x$  values of ca. 1.3% in both samples, reasonably matching the XRD results. We performed SEM-EDS measurements to determine the chloride content in PS2, but in both films and powdered samples we could not achieve reliable values of the Cl concentration as the amplitude of the Cl-related signal was observed to decrease during the measurement.

To model the structural and electronic modifications possibly accompanying Cl-doping, we performed periodic DFT calculations considering a large tetragonal cell initially composed of 32  $\text{MAPbI}_3$  units, see Figure S3, Supporting Information. This allowed us to explore a Cl doping as small as ca. 1% (1 chloride:95 iodide atoms), considering additional values of 0% (corresponding to the pure  $\text{MAPbI}_3$  phase), 4%, 8%, and 33% doping (corresponding to  $\text{MAPbI}_2\text{Cl}$  stoichiometry). Full relaxation of atomic positions as well as of lattice parameters ( $a$ ,  $b$ , and  $c$ ) was performed (see Experimental Section for computational details). We allowed the independent variation of the  $a$  and  $b$  cell parameters, to check whether sizable cell distortions occurred. The  $\alpha$ ,  $\beta$ , and  $\gamma$  cell angles were fixed to 90°. For simplicity we generally considered Cl



substitution to take place in the axial octahedral positions,<sup>23</sup> while for  $x = 4\%$  we considered both axial and equatorial substitutions. Following our previous study we considered for each doping percentage two tetragonal structures (1 and 2), obtained from a different starting arrangement of the organic moieties, see  $x = 0$  structures in Supporting Information Figure S4. Structures 1 and 2 were, respectively, originated by considering a head-to-head (1) and head-to-tail (2) arrangement of the organic molecules. Upon geometry optimization a strong rearrangement of the organic molecules took place for all the investigated structures of type 1, leading to a rather disordered packing, while in structures of type 2 a higher order is maintained, see optimized structures for  $x = 4\%$  in Figure 3 and Supporting Information. The structural and electronic calculated data, reported in Table 1, are fully consistent for  $x = 0\%$  and  $33\%$  with our previous report.<sup>23</sup>

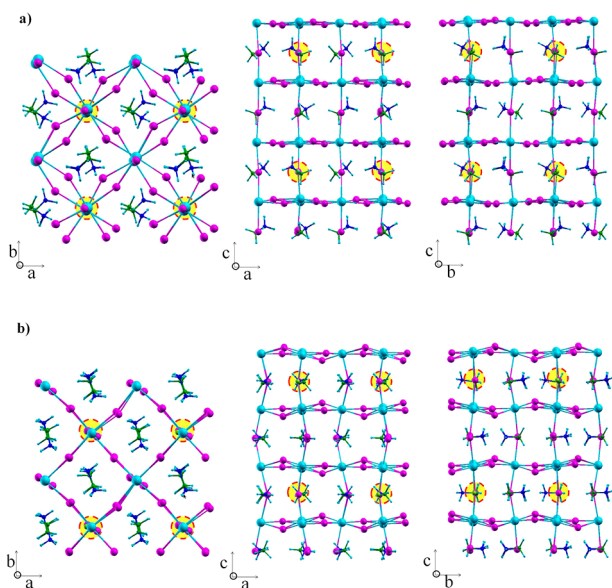


**Figure 3.** Optimized geometries of the 4% chloride-doped  $\text{MAPbI}_{3-x}\text{Cl}_x$  structure 1ax (a) and 2 (b). Three different geometry orientations are shown. The position of the chloride ions is highlighted by yellow circles; Pb = light blue; I = magenta.

For  $x = 0$ , the slightly more stable structure 1 maintains the tetragonal symmetry ( $a = 8.76 \text{ \AA}$  very similar to  $b = 8.75 \text{ \AA}$ ), with calculated lattice parameters in good agreement (within 1.6%) with measured XRD data, as is the calculated band gap. Notice that, as previously mentioned,<sup>23</sup> the agreement on the band gap is most likely fortuitous, being due to the neglect of SOC effects, which possibly compensates for the DFT-PBE band gap underestimate. A recent DFT study on  $\text{MAPbI}_3$  indeed confirmed the relevant role of SOC in reducing the band gap of this material, in an opposite direction to that of the estimated GW correction.<sup>29</sup> This effect is confirmed in the present case: SOC-DFT calculated band gaps are reduced by  $\sim 1 \text{ eV}$  compared to SR-DFT ones; for  $x = 0\%$  and  $4\%$ , the SOC-DFT band gap is  $0.65 \text{ eV}$ , leading to a strong band gap underestimate compared to experimental values. This band gap underestimate is likely to be compensated by GW corrections.

Nevertheless, band gap trends with Cl substitution are expected to be qualitatively accurate,<sup>23</sup> and are supposedly largely independent from SOC effects. This is confirmed by the present results, showing essentially the same band gap for the  $x$

**Table 1.** Optimized Lattice Parameters and Calculated Band Gap (EG) by SR-DFT for Various Cl-Doping Levels<sup>a</sup>

Cl:I (%Cl)	structure	lattice params/2 ( $\text{\AA}$ )	$\Delta V\%$ [ $E_{\text{rel}}$ (eV)]	EG (eV)
0:96 (0.0)	1	<b>8.76, 8.75, 12.74</b>	<b>0.00 (0.00)</b>	<b>1.60</b>
	2	8.71, 9.06, 12.46	+0.68 (+0.04)	1.68
1:95 (1.0)	1	<b>8.76, 8.76, 12.71</b>	<b>-0.12 (0.00)</b>	<b>1.61</b>
	2	8.57, 8.95, 12.61	-0.96 (+0.01)	1.71
4:92 (4.2)	1ax	<b>8.75, 8.77, 12.63</b>	<b>-0.76 (0.00)</b>	<b>1.64</b>
	1ax-eq	8.72, 8.74, 12.69	-0.91 (+0.02)	1.64
	2	8.77, 9.06, 12.26	-0.25 (+0.03)	1.69
8:88 (8.3)	1	<b>8.76, 8.80, 12.53</b>	<b>-1.10 (0.00)</b>	<b>1.74</b>
	2	8.73, 9.12, 11.99	-2.29 (+0.10)	1.66
32:64 (33.3)	1	8.91, 8.84, 11.12	-11.49 (+0.02)	1.96
	2	<b>8.87, 9.03, 11.04</b>	<b>-10.43 (0.00)</b>	<b>1.66</b>

<sup>a</sup>Also, the relative energy of structure 1 and 2,  $E_{\text{rel}}$  (eV), and the volume variation,  $\Delta V\%$ , calculated with respect to the more stable structure 1 with  $x = 0$  are reported. For structure 1 of  $x = 4\%$ , we considered four chloride in axial (1ax) positions and 2axial/2equatorial chloride substitutions (1ax-eq). Boldfaced data refer to the most stable structure for each doping level, corresponding to  $E_{\text{rel}} = 0.00$ .

$= 0$  and  $x = 4\%$  species by both SR- and SOC-DFT calculations. As it can be noticed, we calculate a continuous variation in the lattice parameters (cell volume) and a steady band gap increase with Cl doping, with structure 1 (similar to that of  $\text{MAPbI}_3$ ) being the more stable structure up to  $x = 8\%$ . For  $x = 33\%$  structure 2 becomes more stable, as previously found, with an associated reduction of the band gap. The stability change and band gap reduction observed for structure 2 with  $x = 33\%$  was previously traced by us to the specific hydrogen-bonding interactions between the organic molecules and the inorganic scaffold occurring for structures of type 1,<sup>23</sup> which for  $x = 33\%$  lead to a partly layered structure with consequent increase of the band gap. This is avoided in structure 2, which has a differently distributed hydrogen-bonding pattern.<sup>23</sup>

Most notably, for  $x = 4\%$  we calculate a reduction of the cell volume of 0.76/0.91% (and a slight or null band gap increase, depending on the level of theory) which is strongly correlated to the experimental data, suggesting a Cl incorporation of about 3–4%.

As a preliminary step to the fabrication of the solar cells we performed an SEM investigation on mesoporous  $\text{TiO}_2$  photoanodes filled with the studied perovskite systems and compared the corresponding images with the bare  $\text{TiO}_2$  surface in Supporting Information Figure S2. We found that perovskites appear to be completely penetrated into the mesoporous structure, and no significant difference could be appreciated between the morphologies of the photoanodes sensitized by PS1–3 perovskites.

PS1–3 perovskites were included in solar cell devices, as sketched in the inset of Figure 4, to investigate the influence of chloride doping on their photovoltaic (PV) performances. The solar cells were fabricated on semitransparent fluorine doped tin oxide (FTO) coated glass, coated with a compact  $\text{TiO}_2$  layer that acts as the anode. With the aim of obtaining comparable conditions, the perovskite precursor solution was prepared with the same concentration for the three compounds under examination, infiltrated into the porous oxide mesostructure via spin-coating, and finally dried to enable perovskite formation via self-assembly.

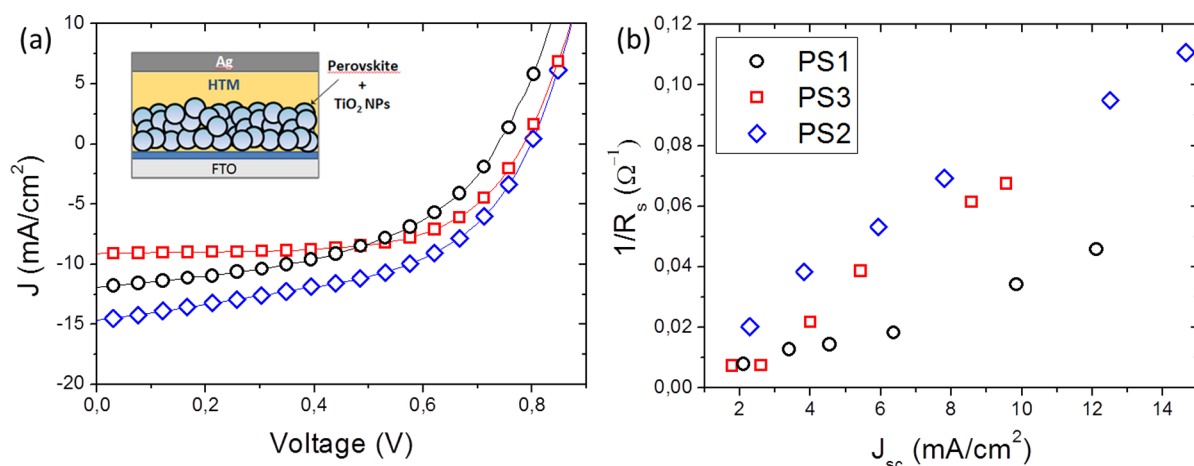


**Figure 4.** *J*–*V* curves under illumination for the PS1–PS3 based hybrid devices. (b) The relationship between reciprocal series resistance and short circuit current density ( $J_{sc}$ ) for the cells fabricated from PS1–3 as light harvesters.  $J_{sc}$  was obtained as a function of light intensity. Inset: a sketch of the hybrid device structure.

In our configuration, the perovskite acts as light harvesters, and spiro-OMeTAD functions as hole collecting/transporting overlying layer. Figure 4a shows the current density/voltage (*J*–*V*) curves of three representative PS1–3 based devices, while the average values are reported in Table 2. The

**Table 2.** Photovoltaic Parameters of the PS1–PS3 Devices

	PCE (%)	FF	$V_{oc}$ (V)	$J_{sc}$ (mA/cm <sup>2</sup> )
PS1	3.85 ± 0.94	0.45 ± 0.16	0.76 ± 0.02	11.65 ± 2.94
PS2	6.15 ± 1.24	0.51 ± 0.09	0.76 ± 0.06	16.36 ± 4.11
PS3	3.85 ± 0.04	0.56 ± 0.06	0.75 ± 0.02	9.23 ± 1.28

differences observed in the device performances, summarized in Table 2, can be directly ascribed to the active materials, since the device architecture remains substantially unchanged for the three perovskites, and reflects our findings in terms of material composition. The increasing  $J_{sc}$  going from PS3 to PS1 to PS2 device can be ascribed to the cooperation of increased light harvesting capabilities and improved charge transport properties. As observed from the spectra reported in Supporting Information Figure S5, the absorption onset is at 750 nm for all the perovskites, consistent with results reported in Figure 2 and DFT calculations; meanwhile, at higher energies the PS2 shows stronger absorption, which in turn results in higher density of photogenerated charge carriers. The  $J_{sc}$  as high as 16.36 mA/cm<sup>2</sup> represents the most relevant difference with the other two compounds. In order to investigate the role of the charge transport on the photovoltaic performances of the three compounds, the series resistance was studied for a set of three representative devices containing the different perovskites as active absorbing layer. The corresponding *J*–*V* curves are reported in Figure 4a. In particular the reciprocal series resistance, calculated as the slope at  $V = V_{oc}$  of the illuminated *J*–*V* curves,<sup>30</sup> was plotted against the short-circuit current for different light intensities.<sup>25</sup> The difference in  $R_s$  in this case will mainly depend on the light harvester layer and in particular on the intrinsic charge transport properties because other factors affecting  $R_s$ , such as electrode resistances and the base contact resistances, will be similar due to the use of same architecture and materials in the cell configuration.<sup>31</sup> Among the factors potentially influencing the resistance, also morphology has been found out to be similar among the examined samples

(Supporting Information Figure S2). Figure 4b shows the  $1/R_s$  trend, and provides evidence of a steeper slope for PS2 and PS3 based cells compared with the cell containing PS1, confirming that charge transport properties are substantially improved by the inclusion of a relatively low amount of chloride in MAPbI<sub>(3-x)</sub>Cl<sub>(x)</sub> in both PS2 and PS3 devices.

## 4. CONCLUSION

In conclusion, we have presented a detailed investigation on I/Cl mixed halide self-assembling perovskites. We showed that Cl incorporation is allowed only at low concentrations (below 3–4%) in I-based perovskites. The strong difference in the halogen ionic radii interferes with the formation of a continuous solid solution. However, even if the material band gap remains substantially unchanged, incorporation of Cl as a dopant dramatically improves the charge transport within the perovskite layer. These findings, in line with previous works suggesting superior transport properties of mixed halide forms MAPbI<sub>(3-x)</sub>Br<sub>x</sub><sup>25</sup> and MAPbI<sub>(3-x)</sub>Cl<sub>x</sub><sup>7</sup> in mesostructured solar cells, demonstrate the beneficial effect given by the copresence of two different halogens inside the perovskite crystalline structure for obtaining a highly conductive light harvesting material. In advance of further developments of super-mesostructured solar cells built on inert scaffolds,<sup>7,15</sup> the employment of a material with improved charge mobility is essential for obtaining competitive photovoltaic efficiencies. Here we demonstrated that the inclusion of a second halogen in the perovskite structure efficiently accomplishes this requirement.

## ■ ASSOCIATED CONTENT

### Supporting Information

Simulated supercell, optimized geometries, and compound absorption spectra. This material is available free of charge via the Internet at <http://pubs.acs.org>.

## ■ AUTHOR INFORMATION

### Corresponding Authors

\*E-mail: andrea.listorti@iit.it (A.L.).

\*E-mail: filippo@thch.unipg.it (F.D.A.).

\*E-mail: mosca@imem.cnr.it (R.M.).

## Notes

The authors declare no competing financial interest.

## ■ ACKNOWLEDGMENTS

S.C., A.L., A.R., and G.G. thank CNR-EFOR, MAAT- PON, BEYOND-NANO-PON, CNRPHOEBUS, for financial support. The authors thank Dr. Massimo Cuscunà for recording SEM images. E.M. and F.D.A. thank FP7-NMP-2009 project “SANS” and CNR-EFOR for financial support. P.F., F.G., F.O., P.F., T.B., G.C., and R.M. acknowledge the support of MIST E-R Consortium.

## ■ REFERENCES

- (1) Lewis, N. S. *Science* **2007**, *315*, 798–801.
- (2) Armaroli, N.; Balzani, V. *Energy Environ. Sci.* **2011**, *4*, 3193–3222.
- (3) Zhou, R.; Stalder, R.; Xie, D.; Cao, W.; Zheng, Y.; Yang, Y.; Plaisant, M.; Holloway, P. H.; Schanze, K. S.; Reynolds, J. R.; Xue, J. *ACS Nano* **2013**, *7*, 4846–54.
- (4) You, J.; Dou, L.; Yoshimura, K.; Kato, T.; Ohya, K.; Moriarty, T.; Emery, K.; Chen, C.-C.; Gao, J.; Li, G.; Yang, Y. *Nat. Commun.* **2013**, *4*, 1446–1455.
- (5) Yella, A.; Lee, H.-W.; Tsao, H. N.; Yi, C.; Chandiran, A. K.; Nazeeruddin, M. K.; Diau, E. W.-G.; Yeh, C.-Y.; Zakeeruddin, S. M.; Grätzel, M. *Science* **2011**, *334*, 629–34.
- (6) Chung, I.; Lee, B.; He, J.; Chang, R. P. H.; Kanatzidis, M. G. *Nature* **2012**, *485*, 486–9.
- (7) Lee, M. M.; Teuscher, J.; Miyasaka, T.; Murakami, T. N.; Snaith, H. J. *Science* **2012**, *338*, 643–647.
- (8) Kim, H.-S.; Lee, C.-R.; Im, J.-H.; Lee, K.-B.; Moehl, T.; Marchioro, A.; Moon, S.-J.; Humphry-Baker, R.; Yum, J.-H.; Moser, J. E.; Grätzel, M.; Park, N.-G. *Sci. Rep.* **2012**, *2*, 1–7.
- (9) Burschka, J.; Pellet, N.; Moon, S.-J.; Humphry-Baker, R.; Gao, P.; Nazeeruddin, M. K.; Grätzel, M. *Nature* **2013**, *3*, 3–7.
- (10) Mitzi, D. B. *J. Mater. Chem.* **2004**, *14*, 2355–2365.
- (11) Mitzi, D. B.; Felid, C. A.; Harrison, W. T. A.; Guloy, A. M. *Nature* **1994**, *369*, 467–469.
- (12) Mitzi, D. B.; Wang, S.; Feild, C. A.; Chess, C. A.; Guloy, A. M. *Science* **1995**, *267*, 1473–6.
- (13) Weber, D. Z. *Naturforsch.* **1978**, *1443*–1445.
- (14) Kojima, A.; Teshima, K.; Shirai, Y.; Miyasaka, T. *J. Am. Chem. Soc.* **2009**, *131*, 6050–1.
- (15) Ball, J. M.; Lee, M. M.; Hey, A.; Snaith, H. J. *Energy Environ. Sci.* **2013**, *6*, 1739–1743.
- (16) Abrusci, A.; Stranks, S. D.; Docampo, P.; Yip, H.-L.; Jen, A. K.-Y.; Snaith, H. J. *Nano Lett.* **2013**, *13*, 3124–3128.
- (17) Park, N. J. *Phys. Chem. Lett.* **2013**, *4*, 2423–2429.
- (18) Kitazawa, N.; Watanabe, Y.; Nakamura, Y. *J. Mater. Sci.* **2002**, *37*, 3585–3587.
- (19) Giannozzi, P.; Baroni, S.; Bonini, N.; Calandra, M.; Car, R.; Cavazzoni, C.; Ceresoli, D.; Chiarotti, G. L.; Cococcioni, M.; Dabo, I.; Dal Corso, A.; de Gironcoli, S.; Fabris, S.; Fratesi, G.; Gebauer, R.; Gerstmann, U.; Gougoussis, C.; Kokalj, A.; Lazzeri, M.; Martin-Samos, L.; Marzari, N.; Mauri, F.; Mazzarello, R.; Paolini, S.; Pasquarello, A.; Paulatto, L.; Sbraccia, C.; Scandolo, S.; Sclauzero, G.; Seitsonen, A. P.; Smogunov, A.; Umari, P.; Wentzcovitch, R. M. *J. Phys.: Condens. Matter* **2009**, *21*, 395502.
- (20) Dal Corso, A.; Conte Mosca, A. *Phys. Rev. B* **2005**, *71*, 115106.
- (21) Toby, B. H. *J. Appl. Crystallogr.* **2001**, *34*, 210–213.
- (22) Poglitsch, A.; Weber, D. J. *Chem. Phys.* **1987**, *87*, 6373–6378.
- (23) Mosconi, E.; Amat, A.; Nazeeruddin, K.; Grätzel, M.; De Angelis, F. *J. Phys. Chem. C* **2013**, *117*, 13902–13913.
- (24) Yamada, K.; Nakada, K.; Takeuchi, Y.; Nawa, K.; Yamane, Y. *Bull. Chem. Soc. Jpn.* **2011**, *932*, 926–932.
- (25) Noh, J. H.; Im, S. H.; Heo, J. H.; Mandal, T. N.; Seok, S. I. *Nano Lett.* **2013**, *13*, 1764–9.
- (26) Im, J.-H.; Lee, C.-R.; Lee, J.-W.; Park, S.-W.; Park, N.-G. *Nanoscale* **2011**, *3*, 4088–93.
- (27) Papavassiliou, G. C.; Pagona, G.; Karousis, N.; Mousdis, G. A.; Koutselas, I.; Vassilakopoulou, A. *J. Mater. Chem.* **2012**, *22*, 8271–8280.
- (28) Qiu, J.; Qiu, Y.; Yan, K.; Zhong, M.; Mu, C.; Yan, H.; Yang, S. *Nanoscale* **2013**, *5*, 3245–8.
- (29) Even, J.; Pedesseau, L.; Jancu, J.-M.; Katan, C. *J. Phys. Chem. Lett.* **2013**, *4*, 2999–3005.
- (30) Qi, B.; Wang, J. *Phys. Chem. Chem. Phys.* **2013**, *8972*–8982.
- (31) Servaites, J. D.; Yeganeh, S.; Marks, T. J.; Ratner, M. A. *Adv. Funct. Mater.* **2010**, *20*, 97–104.